Rapid Transformation of Protein-Caged Nanomaterials into Microbubbles As Bimodal Imaging Agents

Cheng-An J. Lin,[†,⊥,*] Wen-Kai Chuang,[†] Zih-Yun Huang,[†] Shih-Tsung Kang,[∥] Ching-Yi Chang,[†] Ching-Ta Chen,[†] Jhih-Liang Li,[†] Jimmy K. Li,[†,□] Hsueh-Hsiao Wang,[#] Fu-Chen Kung,[△] Ji-Lin Shen,[‡,⊥] Wen-Hsiung Chan,[§,⊥] Chih-Kuang Yeh,[∥] Hung-I Yeh,[#] Wen-Fu T. Lai,[▽,*] and Walter H. Chang[†,⊥,*]

[†]Departments of Biomedical Engineering, [‡]Physics, [§]Bioscience Technology, [⊥]Center for Nano Bioengineering, and Center for Nano-Technology, Chung Yuan Christian University, Chung-Li 32023, Taiwan, [∥]Department of Biomedical Engineering and Environmental Sciences, National Tsing Hua University, Hsinchu 30013, Taiwan, [#]Departments of Medical Research and Internal Medicine, Mackay Memorial Hospital, and Department of Medicine, Mackay Medical College, Taipei 10449, Taiwan, [△]Department of Health Developing and Health Marketing, Kainan University, Taoyuan 33857, Taiwan, and [▽]Graduate Institute of Clinical Medicine, Graduate Institute of Medical Sciences, and Graduate Institute of Biomaterials, Taipei Medical University, Taipei 110, Taiwan. [□]Present address: Medical Device Innovation Center, National Cheng Kung University, Tainan 701, Taiwan.

ABSTRACT

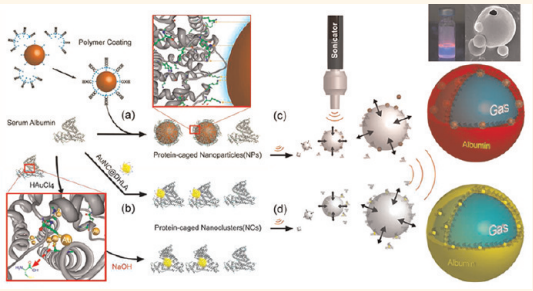

We present a general method for converting colloidal nanomaterials into microbubbles as ultrasound contrast agents. Protein-caged nanomaterials, made either by self-assembled nanoparticles' protein corona or by fluorescent gold nanoclusters, can be rapidly transformed into microbubbles *via* a sonochemical route, which promote disulfide cross-linking of cysteine residues between protein-caged nanomaterials and free albumin during acoustic cavitation. The proposed methods yielded microbubbles with multiple functions by adjusting the original nanoparticle/protein mixture. We also showed a new dual-modal imaging agent of fluorescent gold microbubbles *in vitro* and *in vivo,* which can hold many potential applications in medical diagnostics and therapy.

KEYWORDS: fluorescent gold nanoclusters · quantum dots · ultrasound · microbubbles · protein corona · bimodal imaging

In recent years, various nanoparticles (NPs) have attracted considerable interest in the interdisciplinary research field involving chemistry, physics, engineering, biology, and medicine due to their unique physical properties[1,2] for early detection, accurate diagnosis, and personalized treatment of diseases.[3−6] The most well-studied inorganic nanomaterials including gold NPs, paramagnetic NPs,[7] quantum dots (QDs),[8,9] and fluorescent gold nanoclusters (AuNCs)[10−13] can be used as contrast agents for medical imaging of computed tomography (CT),[14] magnetic resonance imaging (MRI),[15−18] or fluorescence-based imaging.[19−22] Among all imaging modalities, no single modality is sufficient to obtain all the information.[2,23] NPs have large surface areas where many functional moieties can be incorporated for multimodality imaging. The combination of MR-detectable and near-infrared fluorescent (NIRF) nanoprobes was investigated for *in vivo* tumor imaging,[24,25] apoptosis,[26] or atherosclerosis.[27,28] Other dual-modality nanoprobes for PET/optical,[29] MRI/optical,[30−32] and SPECT/MRI[33] imaging have also been demonstrated either *in vitro*, *ex vivo*, or *in vivo*. Ultrasound (US) contrast technique has recently raised great interest not only because the contrast agents used are of lower cost but also because it eliminates the need to handle radioactive materials and offers convenience for monitoring patients. Commercially available ultrasound contrast agents comprise gas-encapsulated microbubbles (MBs, ∼1−10 μm), which enhance transiently backscattered acoustic signals, due to the large impedance mismatch between the MBs and the tissues, and enable resonant scattering.[34−36] In addition to successful use of MBs in clinical diagnostic imaging (B-mode ultrasound image, harmonic imaging, phase inversion imaging),[37−39] multifunctional MBs carrying drug-loaded NPs are successfully applied in preclinical studies, including thrombi,

* Address correspondence to chengan_lin@cycu.edu.tw (C.-A.J.L.), whchang@cycu.edu.tw (W.H.C.), laitw@tmu.edu.tw (W.-F.T.L.).

Received for review February 21, 2012 and accepted May 18, 2012.

Published online May 18, 2012
10.1021/nn300768d

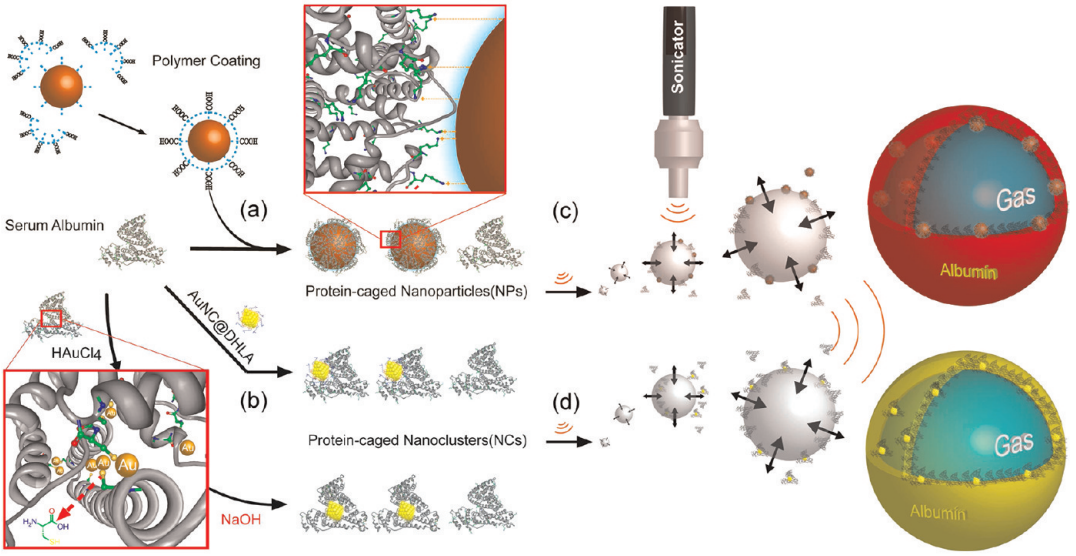

Figure 1. Synthesis of protein-caged nanomaterials toward dual-functional microbubbles (MBs). In the left column the synthesis of the protein-caged nanomaterials is shown. (a) Nanoparticles (NPs) with hydrophobic capping are coated with amphiphilic poly(isobutylene-*alt*-maleic anhydride) derivatives, giving NP surfaces a universal negative charge in aqueous buffer (left, top). The polycorboxylate-functionalized NPs can rapidly induce serum albumin to the self-assembled monolayer on each NP (protein-caged NPs) through complementary electrostatic interaction. The inset in (a) illustrates that the lysine-rich domain of albumin could be electrostatically adsorbed onto the NP. (b) As-prepared fluorescent gold nanoclusters (AuNC@DHLA) can directly induce serum albumin to electrostatically self-assemble into a complex. Another method for synthesizing protein-caged nanoclusters (NCs) is the "biomineralization" process, in which gold ions ($AuCl_4^-$) are adsorbed onto protein and are reduced to NCs *in situ* at the physiological temperature of basic solution (left, bottom). The inset in (b) illustrates that gold ions could bind strongly with free cysteine residues during nucleation. The right column illustrates the dual-functional MBs made from these protein-caged nanomaterials. Ultrasound-generated cavitation and superoxide radicals could induce cross-linking of protein-caged nanomaterials with free albumin at the air−water interface, resulting in stable (c) NP- or (d) NC-coated MBs, which comprise an echogenic core with a functional shell.

atheroma plaques, and tumors, with ultrasound-triggered bubble disruption and subsequent drug release.[40−46] Further improvement in the accuracy of clinical assessment of a disease can be achieved by combining US with other imaging modalities such as fluorescence or MRI imaging.[30,47−49]

Multiple imaging modalities are realized by immobilizing QDs, iron oxide, and gold NPs to the shell of MBs.[48−50] Currently, MBs coated with NPs are produced in a multistep procedure, which involves sonication of a NP and oil mixture in the presence of a gas and subsequently transferring the bubbles into an aqueous solution.[48,51] Alternatively, NPs can be attached to the surface of bubbles in a layer-by-layer deposition process.[49,52] A microfluidic strategy has recently enabled the synthesis of monodisperse NP-loaded bubbles *via* the formation of double emulsions[50] or a multistep[53] or single-step[54] LbL process, which are complicated, low-yield, and/or time-consuming. The development of an efficient, single-step method for producing monodisperse MBs loaded with NPs is highly desirable.

Herein, we report for the first time a facile ultrasonic approach to producing protein-caged nanomaterials coated with MBs as bimodal contrast agents. Two types of protein-caged nanomaterials, which are prepared either by a self-assembled protein corona around polymer-coated nanoparticles (referred to here as protein-caged NPs) or by protein-caged fluorescent gold nanoclusters (referred to here as protein-caged NCs), can be rapidly transformed into MBs by high-intensity ultrasound-induced emulsification and cross-linking of protein-caged nanomaterials with a common commercially available protein, bovine serum albumin (BSA), in aqueous solutions (Figure 1). The sonochemical route produces MBs with a mean diameter of 1−3 μm, which can safely pass through the microvasculature without diffusing across the endothelium.[54] The morphological transformation of versatile nanomaterials into MBs, which comprise a gas core surrounded by a biocompatible protein/NP shell, forms nanomaterials with the extra ability to scatter sound waves, offering them another modality potential in clinical application[55,56] as ultrasound contrast agents. Larger bubbles possess better scattering ability since the intensity of scattering for nonresonant gas bubbles is proportional to the sixth power of the radius of the bubble.[57] The rapid and simple process generates monodispersed MBs with decent stability of at least one month (Table S2). The shell materials of MBs can be "tailor-made" by initial concentration or type of protein-caged nanomaterial solution, which has been demonstrated by QDs as well as iron oxide nanoparticles (FeNPs). The NP-loaded capacity is assessed

via confocal microscopy as well as flow cytometry. This study also highlights the importance of thiol content in the protein-encapsulated fluorescent AuNCs for the ultrasonic synthesis of US/NIRF dual contrast agents. Furthermore, we show the proof-of-concept experiments of the NP-functionalized MBs as imaging agents *in vitro* and *in vivo*. This research hereby focuses on a detailed characterization of practically important parameters rather than on understanding the underlying mechanisms.

RESULT AND DISCUSSION

Protein-Caged Nanoparticles. Figure 1a shows the schematic of the protein-caged NPs used in the present work. A general surface is required before forming the protein-caged NPs. We have previously demonstrated that an amphiphilic polymer coating can efficiently transfer different hydrophobic nanoparticles into the aqueous solution, offering them a universal surface for biomedical application.[58] According to the polymer coating strategy,[58,59] hydrophobic NPs (CdSe/ZnS QDs, Au or Fe_3O_4 NPs) in chloroform were first mixed with an appropriate amount of 75% dodecylamine-modified poly(isobutylene-*alt*-maleic anhydride), followed by a slow evaporating procedure to remove all the chloroform, and finally dissolved in borate buffer solution (see details in the Supporting Information). The hydrophobic portion of such amphiphilic polymer intercalated with the hydrophobic surfactant on the NPs and the hydration/deprotonization of maleic anhydride backbone stabilizes the NPs in the aqueous buffer by electrostatic repulsion. The bands on the gel electrophoresis of each polymer-coated NPs (Figure 2) are remarkably narrow, indicating a homogeneous distribution of size and charges. Upon mixing with a high concentration of BSA solution (50 mg/mL), all the polymer-coated NPs were significantly retarded on the gel electrophoresis, which is attributed to the formation of the self-assembled nanoparticle−protein corona. We conducted a series of experiments for confirming the corona formation and activity. If polymer-coated NPs mixed with the series of diluted BSA solution, the initial self-assembled NPs with one or two BSA biomolecules could be separated using gel electrophoresis (Figure 2a and Supporting Figure S4). The surface plasmon absorption peak of gold NPs did not result in any red-shift even in the most concentrated BSA solution, indicating no protein-induced agglomeration[60,61] in these polymer-coated NPs (Supporting Figure S6). The purified NP/protein corona mixing with bare polymer-coated gold NPs showed no cross-linking effect and can be easily separated by gel electrophoresis (Supporting Figures S5, S6 and Figure 2b). In addition, all NP−protein corona extracted from the gel showed absorption characteristics of both corresponding NPs and proteins (280 nm). Further evidence was found in the negative-stain TEM image of core−shell binding complexes of polymer-coated NPs with BSA proteins, *i.e.*, the clear, unstained layer around the NPs (Figure 2c). In the presence of excess proteins, all the NPs with a polycarboxylate surface were encapsulated by proteins, showing a high binding efficiency in a core-independent manner.

Conversion of Protein-Caged NPs into MBs. The first air-encapsulated MB agent approved for human use by the U.S. FDA in 1994 was formed by sonication of 5% serum albumin,[36,62] which is highly biocompatible. We have shown in Figure 2 that polymer-coated NPs can quickly form NP−protein corona *via* mixing in a 10% BSA solution. When the mixture solution was irradiated with high-intensity ultrasound (Branson, 20 kHz, 3 mm microtip horn) for 30 s at an acoustic power of 200 W cm^{-2}, the as-prepared NP-coated MBs were separated from the remaining proteins and NPs by flotation and repetitive washing. By using QDs as an example, the sonication-induced MBs contain a total of about 2×10^8 bubbles/mL of suspension with a mean diameter of approximately 1 μm (Figure S23). Figure 3 shows the typical floating property and confocal fluorescence microscopy images of the MBs loaded with green-emitting QDs (gQD: QD-520) or red-emitted QDs (rQD: QD-610). MBs are shown to comprise a gaseous core (dark) and a strong fluorescent shell when excited at 488 nm (Figure 3b). The mechanism responsible for the formation of NP-coated MBs is the combination of two ultrasound-induced phenomena: emulsification and cavitation.[63] Sonication might induce intermolecular disulfide cross-linking between NP−BSA corona and free BSA proteins at the air−water interface, caused by the superoxide radicals generated during acoustic cavitation.[64] To further assess the loading potency, MBs were examined by flow cytometry, the results of which showed more than 90% of MBs loaded with QDs (Figure 3c).

It is also possible to load two kinds of NPs onto the shell of MBs at the same time. To demonstrate this idea, equal amounts of gQD and rQD mixed in 7.5% BSA solution rapidly form protein-caged NPs, which were then transformed into MBs upon irradiation with a high-intensity ultrasound. Purified MBs with/without quantum dots were assessed by flow cytometry analysis with two emission detectors, *i.e.*, FL1-H channel (515−540 nm) and FL2-H channel (564−606 nm). Both gQD and rQD can be excited by a 488 nm laser and emit two separable fluorescent spectra with peak at 520 and 610 nm, respectively. As seen in Figure 3c, the quantum dot-free MBs showed few detected signals in both emission channels. MBs produced from a QD/BSA mixture presented only single, intense signals between the two channels. However, MBs produced from gQD/rQD (1:1) mixtures showed intense signals in both channels, indicating the existence of two kinds of QDs on each microbubble.

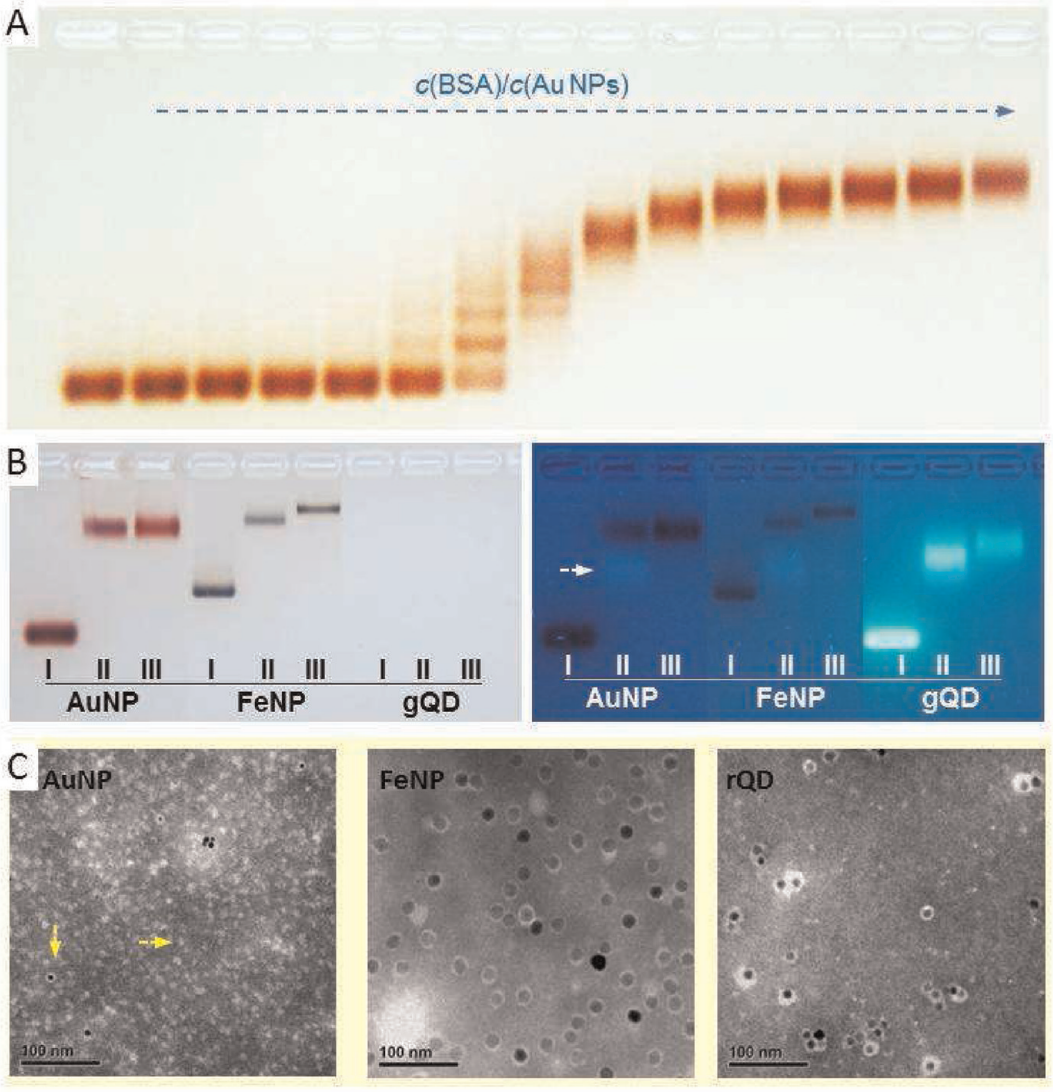

Figure 2. Gel electrophoresis and TEM imaging of protein-caged NPs. (a) Bovine serum albumin (BSA) molecules were electrostatically attached to polymer-coated 6 nm gold NPs (AuNPs). The number of BSA molecules attached per AuNP was adjusted by changing the concentration of BSA (*c*(BSA)) in the following range: *c*(BSA)/*c*(Au NPs) = 0, 0.04, 0.09, 0.2, 0.4, 0.7, 1.4, 3, 6, 12, 23, 46, 94, 188, and 375. Gel electrophoresis was performed on 2% agarose gels for 90 min. The lanes, from left to right, show samples with increasing BSA concentration. The AuNPs grow in size and become more retarded on the gel due to the attachment of more BSA molecules with increasing *c*(BSA)/*c*(AuNPs) ratio. (b) Gel electrophoresis of different polymer-coated NPs, such as AuNPs (6 nm AuNPs), iron oxide NPs (15 nm FeNPs), and green-emitting quantum dots (gQD), before (I) and after (II) mixing with 50 mg/mL BSA molecules. Images are taken under white light (left) or UV lamp excitation (right). The purified NPs/BSA complexes (III) are also included. The arrow indicates the fluorescence of unattached free BSA molecules, which disappear upon purification. (c) TEM image of the protein corona layer obtained by negative staining with 2% phosphotungstic acid at pH 7. The NPs (dark core) seem to be surrounded by a white disk of unstained proteins that stands out against the stained background. The images from left to right are unpurified AuNP, purified FeNP, and red-emitting CdSe/ZnS QDs (rQD), respectively. The white spots within the AuNP image are contributed by unstained BSA molecules. A Hitachi H-7100 was operated at 80 kV. Scale bar: 100 nm.

Protein-Caged Nanoclusters. Protein-caged fluorescent AuNCs used in the present work can be formed by either self-assembly or "biomineralization", which is gold ions adsorbing onto a nucleation site and mineralizing within the "protein cage" at the physiological temperature. Ultrasmall fluorescent gold NCs (or AuNCs),[65] whose size typically ranges from subnanometer to approximately 2 nm (core diameter), have recently become a promising biomedical nanomaterial because they contain no toxic heavy metals, in contrast to CdSe/ZnS QDs.[66,67] We have previously reported fluorescent AuNCs synthesized by precursor-induced etching of didodecyldimethylammonium bromide (DDAB)-stabilized gold NPs, resulting in high red luminescence upon ligand exchange with dihydrolipoic acid (DHLA) for transfer of the product to aqueous solution.[10] DHLA-protected AuNCs (AuNC@DHLA) can also form a complex with BSA proteins (AuNC@DHLA^{BSA}) *via* electrostatic adsorption, as assessed by gel electrophoresis (Figure 4 and Figure 1b).

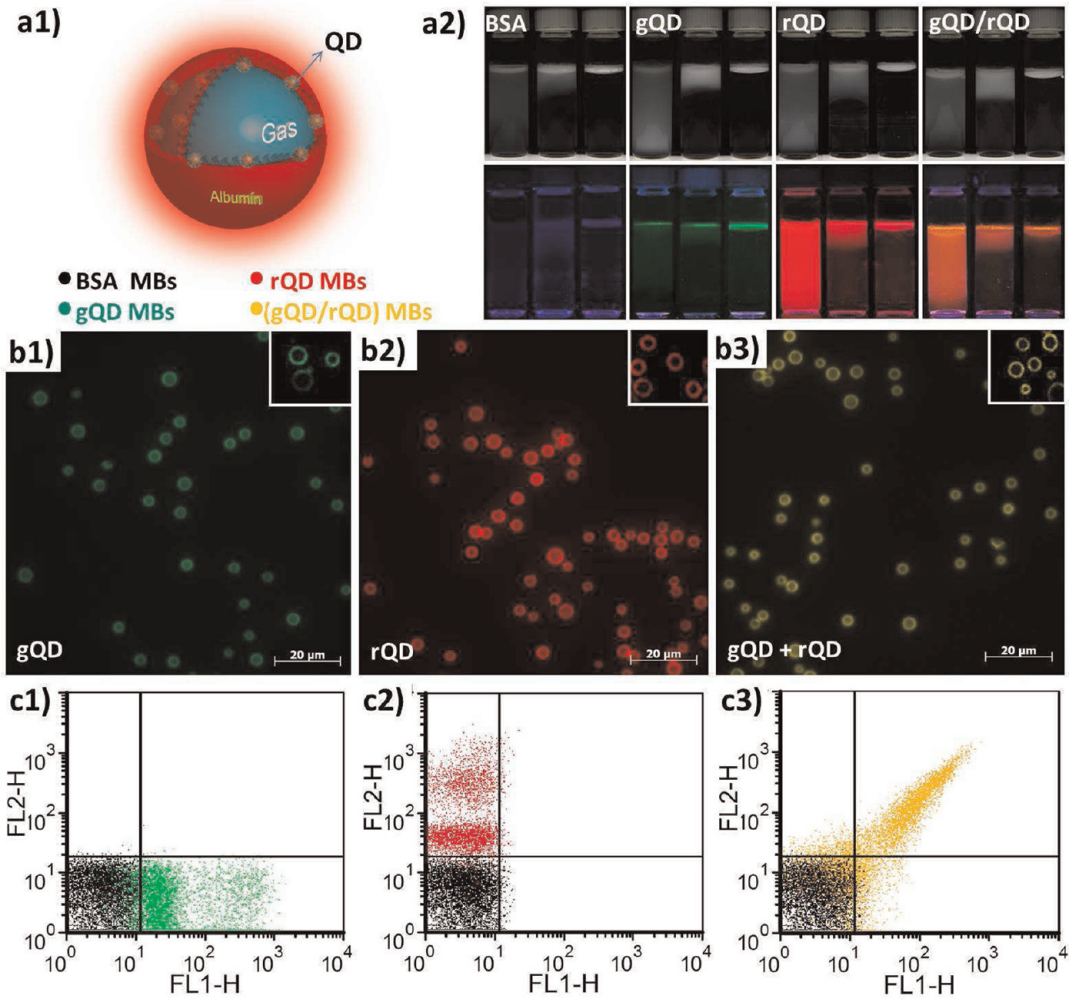

Figure 3. (Row a) Scheme (a1) and time-correlated floating imaging of quantum dot (QD)-coated microbubbles (MBs) under daylight (a2) and UV lamp (a3). Fluorescent imaging (row b) and flow cytometry (row c) analysis of different QD-coated MBs, which were prepared *via* a one-pot sonochemical protocol. MBs were produced from 75 mg/mL of BSA solution containing 0.5 μM gQDs (b1, c1) or rQDs (b2, c2) or a gQD/rQD mixture (b3, c3). Confocal microscopy images of QD-coated MBs (inset) were obtained by 488 nm excitation with 505 nm long-pass emission and labeled with pseudocolors in green, red, and yellow, respectively. The scale bars are 20 μm. For quantitative analysis of flow cytometry (row c), all MBs carrying different QDs were excited at 488 nm, and fluorescence signals from individual MB were collected through two band-pass filters, *i.e.*, FL1-H channel (515−540 nm) and FL2-H channel (564−606 nm). For comparison, a control group of MBs made from 75 mg/mL of BSA solution was also analyzed by flow cytometry (labeled in black).

Dark field images of an unstained, freeze-dried protein−NC complex of AuNC@DHLA^{BSA} were recorded using a scanning transmission electron microscope (STEM facility at the Brookhaven National Laboratory) operating at 40 kV. High-angle annular dark field (HAADF) STEM analysis indicated that the main complex formed comprised protein monomers on AuNCs with an average size of 1 nm (Figure 4d). Fluorescent AuNCs can be synthesized directly by a simple process similar to the biomineralization behavior that was first described by Ying's group.[68] Upon adding gold ions ($AuCl_4^-$) to protein solutions such as BSA and lysozyme, the protein molecules sequester gold ions *via* electrostatic force (see Figure 1B), followed by a reduction of the gold ions partially through functional ligands, which may in turn enhance the binding affinity of the gold ions. Cysteine-rich proteins could provide a strong binding affinity with gold ions. Au^{3+} ions are more easily reduced to Au^0 or Au^+ at basic pH than those at physiological pH.[69] Therefore, the entrapped ions are progressively reduced to form fluorescent AuNCs *in situ* by changing the reaction pH to basic under physiological temperature. More than 5% of cysteine (Cys) content in BSA (35 Cys/monomer) and in lysozyme (8 Cys/monomer) might dominate the successful formation of red-fluorescent AuNCs with a maximum intensity located at λ_{max} = 650 nm through a biomineralization process (Figure 4b and also see details in the Supporting Information).

Conversion of Protein-Caged AuNCs to Fluorescent MBs. Protein-caged fluorescent AuNCs were formed by either self-assembly of AuNC@DHLA with proteins (AuNC@DHLA^{BSA}) or intramolecular "biomineralization" of gold NCs in proteins (AuNC@BSA, AuNC@lysozyme).

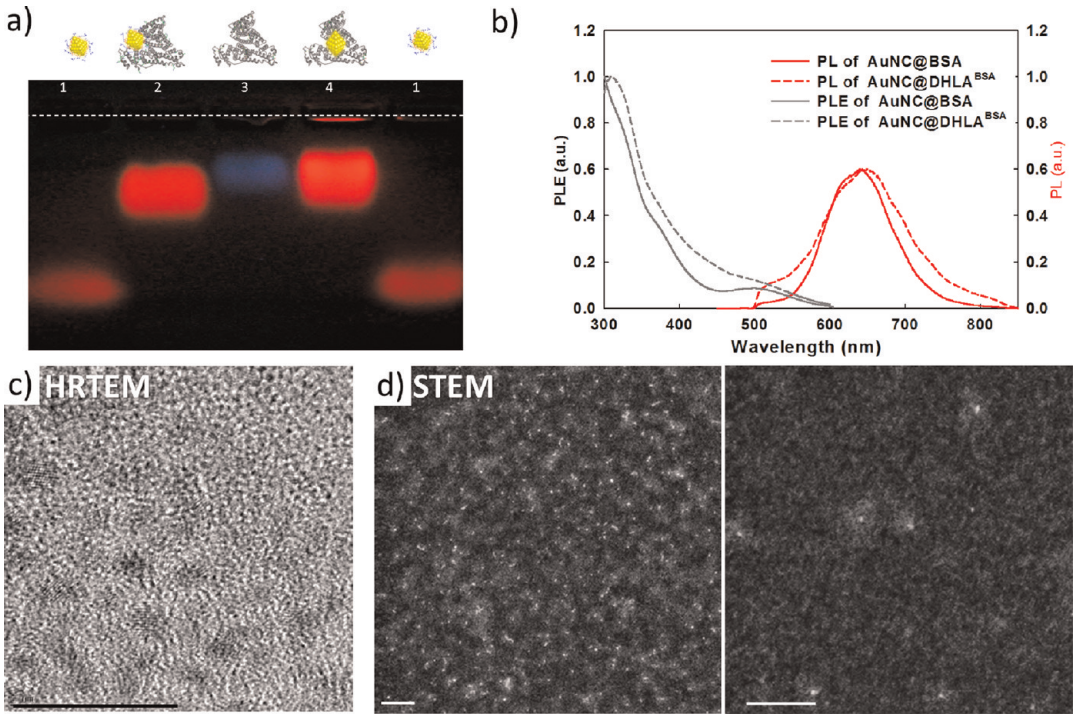

Figure 4. (a) Electrophoretic mobility of gold nanoclusters (NCs) in 2% agarose gels (7.5 V/cm electric field, 25 min running time). DHLA-protected AuNCs and BSA molecules were run as controls in lanes 1 and 3. Lane 2 shows the result from mixing AuNC@DHLA and BSA, *i.e.*, AuNC@DHLA^{BSA}. Lane 4 shows the samples from biomineralized AuNCs with BSA molecules, *i.e.*, AuNC@BSA. (b) Photoluminescence (PL, red) and photoluminescence excitation spectra (PLE, gray) of AuNC@DHLA^{BSA} (solid line) and AuNC@BSA (dashed line). For the PL spectrum, excitation at 488 nm was used. For the PLE spectrum, a fixed emission at 650 nm was used. (c) High-resolution TEM and (d) HAADF STEM images of BSA molecule attached to ~1.5 nm AuNCs (*i.e.*, AuNC@DHLA^{BSA}), which were isolated using gel electrophoresis and ultracentrifugation. STEM imaging clearly recorded the complex structure of AuNC@DHLA^{BSA} comprising the unstained protein (pale scattering) and AuNC (strong scattering dots), in contrast to TEM images showing only the imaging of AuNCs. Scale bar: 10 nm.

Free cysteine residues in the protein-caged AuNCs are assumed to be an important requirement for the production of stable fluorescent MBs. To prove the concept, different BSA-caged or lysozyme-caged AuNCs mixed with an equal amount of 10% BSA are selected to prepare air-filled MBs by following the standard sonochemical process and discarding the remaining protein-caged NCs by flotation/washing steps. Figure 5 shows the confocal and fluorescence microscopy images of the fluorescent MBs coated with protein-caged AuNCs. The sonochemical route can successfully induce fluorescent AuNC-coated MBs except in the case of AuNC@lysozyme, assessed by confocal imaging and flow cytometry (Figure 5a, c). The correlation between size and red emission of AuNCs (AuNC@BSA) indicates a distribution of around 25 Au atoms capped by cysteine residues of BSA molecules with only a small amount of Au(I) present on the surface of the Au core.[68] Similarly, the six cysteine groups in each lysozyme molecule of AuNC@lysozyme, which are less prevalent on the shells of MBs, could be used only to protect the AuNCs, in contrast to AuNC@BSA, presenting 35 thiols groups that protect the NCs as well as cross-link with other proteins on the microbubble shells. The data also were in agreement with the fluorescent microscopy results (Figure 5b).

Test of Dual-Modal Ability Using NC-Coated MBs. For clinical applications, the size of the MBs should be controlled preferably to around 3 μm.[70] As shown above, NP-coated MBs produced by high-intensity ultrasound in this study have significantly reduced the process time. In addition, their size (1−5 μm) was smaller than the dimensions of the pulmonary and systemic capillaries and that of MBs fabricated by microfluidic methods,[54] in which the NP-loaded bubbles (5−20 μm) were generated at a low frequency of 700 bubbles/s, although they had better size distribution. From previous reports, NP-loaded MBs not only can intensify nonlinear ultrasound imaging signals due to their resistance to compression[54] but also offer another imaging modality for photoacoustic,[71] fluorescent imaging[49] or MRI[48,54,72] in comparison with MBs without NPs. Herein, we introduced for the first time the proof-of-concept for bimodal ability of fluorescent MBs coated with protein-caged AuNCs. Fluorescent AuNCs not only can be used as biocompatible markers for *in vitro*[10] and *in vivo*[65] labeling but can also offer good contrast in NIR fluorescence imaging *in vivo*.[73] We proved the concept of AuNC@DHLA-coated MBs in two imaging modalities: an *in vivo* optical imaging system (Xenogen IVIS 200) and a clinical diagnostic ultrasound imaging system (CGMC OPUS 5000). The

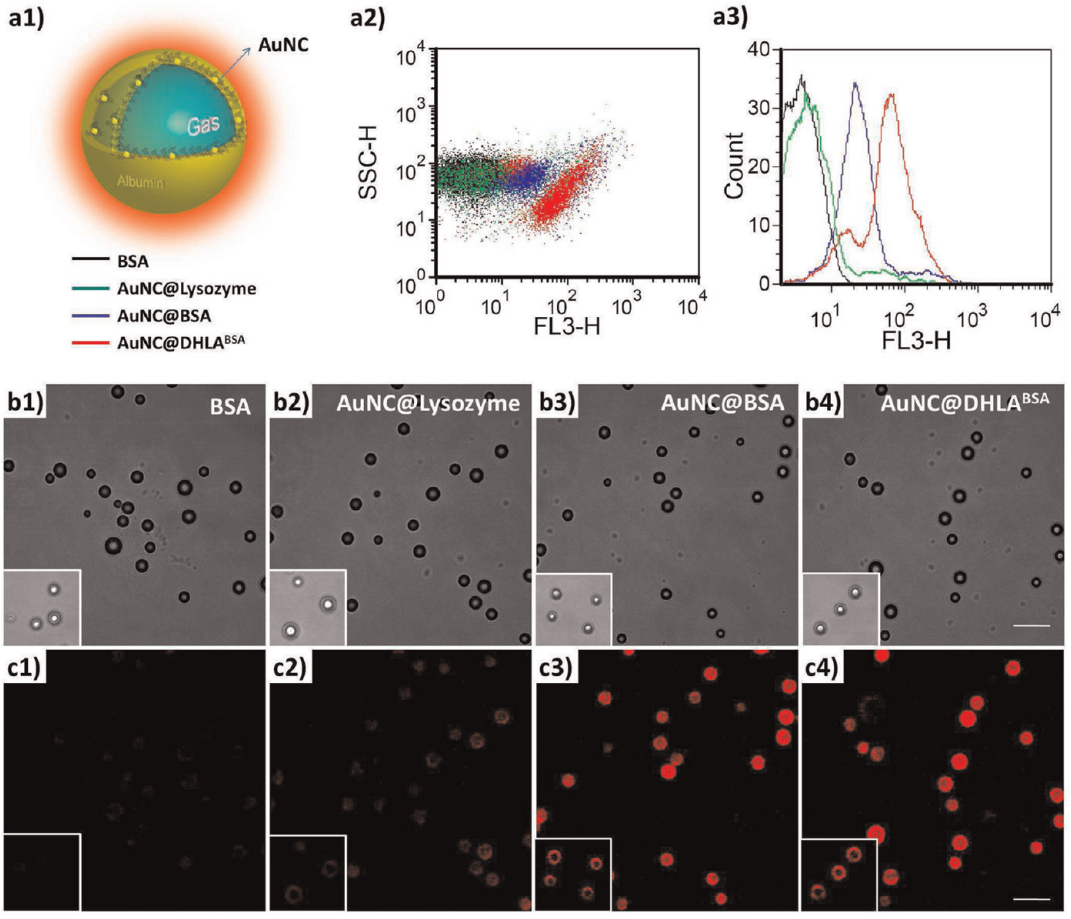

Figure 5. Optical properties of MBs produced from different protein-caged AuNC solutions. (Row a) Scheme and flow cytometry histograms of MBs carrying different AuNCs excited at 488 nm, and fluorescence signals from individual MBs collected through a long-pass filter (FL3-H channel, >650 nm). (a2) Scattering signals *versus* fluorescent intensity. (a3) Counts *versus* fluorescent intensity recorded from MBs produced from 50 mg/mL of BSA solution containing 10 μM AuNC@Lysozyme, AuNC@BSA, and AuNC@DHLA^{BSA} through a one-pot sonochemical protocol. (b) Morphology and (c) fluorescence imaging of MBs carrying different AuNCs, obtained by inverted microscopy labeled with pseudocolor in red. Confocal microscopy images of NC-coated MBs (inset) were obtained by 488- nm excitation with 505 nm long-pass emission. Note that all of the confocal images were equally corrected for brightness and contrast. The scale bars are 20 μm.

NP-loaded MBs produced from 0, 25, 50, and 100 μM AuNC@DHLA in 10% BSA solution were suspended in water and placed in a 1 cm well of 1.5% agarose gel. Figure 6a shows *in vitro* ultrasound images of the dispersion of NC-free and NC-coated MBs. A strong contrast ultrasound image signified a strong echogenic signal for NC-coated MBs as well as NC-free MBs. Contrast intensity was then significantly reduced upon ultrasound-induced destruction of the MBs through prolonged exposure to ultrasound imaging (30 min).[54,74] Furthermore, Figure 6b presents fluorescence reflectance images of different surface densities of AuNC@DHLA^{BSA} on the same MBs (10^7 bubbles/mL). MBs carrying a higher amount of fluorescent Au NCs exhibited enhanced photoluminescence intensity, as shown by the quantified color images. In contrast to ultrasound imaging, the fluorescent signals of NC-coated MBs display no significant difference from the ones subjected to ultrasound-induced destruction. Similar results appeared in *in vivo* imaging (Figure S25).

A NC-coated MB solution (200 μL) was subcutaneously injected into BALB/c nude mice, and the *in vivo* imaging was performed immediately after ultrasound-induced destruction of MBs. NC-coated MBs without destruction (close to left hind limb) showed intense signals in both US and IVIS modalities, but the disrupted NC-coated MBs in proximity to the right hind limb lost the ability to produce contrast US imaging. In our further characterization of MBs under ultrasound exposure (Figure S27, S28), the contrast enhancement of MBs was 11−12 dB under the condition of acoustic pressures below 0.8 MPa. Increasing the acoustic pressure to higher than 0.8 MPa significantly decreased the contrast enhancement, indicating the occurrence of MB destruction. The acoustic pressure of 1 MPa, at which the contrast enhancement decreased to about half the original level, can be referred to as the destruction threshold of MBs. For comparisons, our previous study showed that the commercial lipid-based MBs SonoVue can be thoroughly disrupted

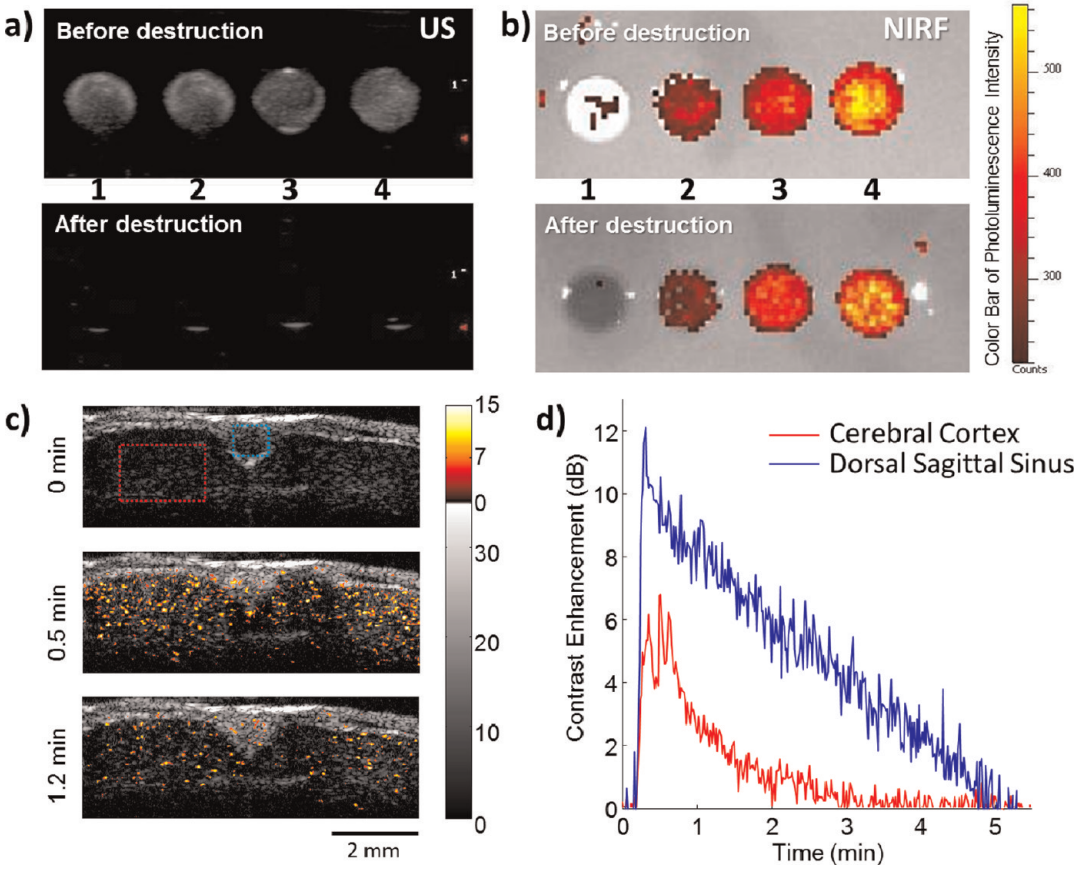

Figure 6. (a) Bimodal imaging of fluorescent AuNC-coated MBs "before" and "after" ultrasound-induced MB destruction. MBs produced from 100 mg/mL of BSA solution containing 0, 25, 50, and 100 μM AuNC@DHLA (left to right: 1, 2, 3, and 4) loaded in a 1% agarose well (diameter/height: 1 cm/1.5 cm) contained 10^7 bubbles/mL. *In vitro* ultrasound imaging was performed by using a mechanical index of 0.5 and frequency of 7.5 MPa. Each MB loaded in a 1% agarose well (diameter/height: 1 cm/1.5 cm) contained 10^7 bubbles/mL. All contrast-enhanced ultrasound imaging signals were significantly reduced after destruction of MBs induced by prolonged exposure of ultrasound imaging (30 min). (b) Fluorescence reflectance images (excitation filter, 500/30 nm, and emission 700/20 nm) of MBs containing different surface densities of AuNC@DHLA, the same as the samples with *in vitro* ultrasound imaging. Related fluorescent intensity is labeled with a color bar of photon counts. (c) B-mode images at different time points, and (d) time−intensity curves for a rat brain with the skull removed after an intravenous injection of MBs. The B-mode images are demonstrated with a color-coded overlay to represent the spatial distribution of MBs. The time−intensity curves were analyzed for two regions of interest, in the dorsal sagittal sinus and left cerebral cortex.

under similar insonation conditions but at an acoustic pressure of 400 kPa.[75] One difference lies in the thick shell of around 20−30 nm, compared with ~5−10 nm for lipid-based MBs, as measured from the SEM image (Figure S22). These results suggested that the NC-coated MBs would be suitable for US/NIRF imaging as well as ultrasound-triggered MB disruption toward drug release.[40−46]

We also investigated the contrast-enhancing ability of NC-coated MBs in a rat brain with the skull removed. The experiment was conducted using a self-developed high-frequency (40 MHz) ultrasound imaging system, as shown in Figure S26.[76] Figure 6c shows the B-mode images of the brain with the skull removed at different time points after the injection of MBs. Local variations in image contrast extracted by a high-pass interframe filter are demonstrated as a color-coded overlay to represent the spatial distribution of MBs. Time−intensity curves were analyzed for two regions of interest, selected in the dorsal sagittal sinus and left cerebral cortex. The results are shown in Figure 6d and the Supplementary video (Video S1). The rapid rise and relatively slow falling rates in contrast enhancement indicate the wash-in and wash-out phases of MBs, respectively. A maximum contrast enhancement of 12 dB was measured in the dorsal sagittal sinus. The MBs also flowed into the capillary bed and clearly enhanced the contrast in the left cerebral cortex by up to 6−7 dB.

CONCLUSION

We have described a simple method for producing MBs coated with various types of NPs. We have also reported the general route for synthesizing protein-caged nanomaterials, which can be used for producing bimodal US contrast agents. Our previously reported amphiphilic polymer, poly(isobutylene-*alt*-maleic anhydride) derivatives, not only can transfer hydrophobic NPs to aqueous solution but can also offer a universal surface for self-assembly of NPs with serum proteins,

which yields the first type of protein-caged nanomaterials: a core–shell complex of NP protein corona. The polycarboxylate polymer was used successfully for linking inorganic colloidal NPs of different materials (Au, CdSe/ZnS, Fe_3O_4) to BSA protein corona. The polymer-coated NPs with size ranging from 2.5 to 15 nm demonstrated the universality of the approach, in which the formation of the protein corona is only mediated by the electrostatic interaction and does not depend on the core materials and size. Protein-caged AuNCs, the second type of protein-caged nanomaterials, can be synthesized by intraprotein "biomineralization" or self-assembly of AuNCs with proteins, thus resulting in high photoluminescence in red to near-infrared emission. Both types of protein-caged nanomaterials can be rapidly converted into MBs by a simple and straightforward sonochemical route. The MBs thus obtained exhibit a small size as well as long-term stability, due to intermolecular disulfide cross-linking between protein-caged nanomaterials and free BSA proteins during acoustic cavitation. The free thiol residues in protein-caged nanomaterials dominated the formation of nanomaterial-coated MBs, evidenced from the rare formation of MBs upon sonication of AuNC@lysozyme protein mixtures. Further, the functionalization of MBs can be easily achieved by adjusting the original NP/protein mixture. We also demonstrated different imaging modalities with biocompatible AuNC-coated MBs, used in conjunction with both *in vitro* and *in vivo* ultrasound and fluorescent imaging. Finally, this general method of rapid conversion of versatile nanomaterials into MBs might have many potential applications in medical diagnostics and therapy, such as targeted diagnostic imaging and drug and gene delivery.[39,55,56,70,77]

METHODS

Experimental Setup of Ultrasound Brain Imaging. We performed ultrasound imaging of a rat brain with the skull removed to observe the echogenicity of AuNC@DHLA-coated MBs. The experiment was conducted using a self-developed high-frequency ultrasound imaging system equipped with a single-element 40 MHz $LiNbO_3$ ultrasound transducer, as shown in Figure S26.[76] In brief, a two-dimensional motor (model HR8, Galil Motion Control Inc., CA, USA) and a motion controller (model DMC-2160, Galil Motion Control Inc., CA, USA) were used to regulate the position of the transducer. An anesthetized Sprague–Dawley rat was placed below the transducer, with the skull removed (approximately 1×1 cm^2) for ultrasound transmission. As the transducer scanned over the brain, three-cycle pulses were generated by an arbitrary waveform generator (model AWG 2040, Tektronix, CA, USA) and amplified by a 50 dB power amplifier (model 325LA, E&I, NY, USA) to drive the transducer at an acoustic pressure of 2.4 MPa. The same transducer received acoustic echoes from the brain through a diode limiter/transformer diplexer circuit (model DIP-3, Matec Instruments NDT, MA, USA). The received signals were amplified by a preamplifier (model AU-1114, MITEQ Inc., NY, USA) and then digitized by a 12-bit analog-to-digital board (model CS12400, Gage Applied Tech Inc., IL, USA) at a sampling rate of 400 Msamples/s. A counter/timer board (model PCI-6602, National Instruments, TX, USA) synchronized all triggers with the sampling clock to eliminate trigger jitter. Acquired data were processed off-line into B-mode images using MATLAB (MathWorks Inc., MA, USA) software. During the experiment, MB solution (600 μL) at a concentration of 5×10^7 MBs/mL was injected through the right jugular vein. A series of B-mode images were then acquired at a frame rate of 1 fps to monitor the perfusion of MBs.

Conflict of Interest: The authors declare no competing financial interest.

Acknowledgment. The authors gratefully acknowledge the financial support from the National Science Council of Taiwan (NSC 100-2120-M-038; NSC 100-2627-M-033). The authors also thank Miss Ying-Hsiu Liu for the help in reproducing works. STEM images were assisted by Prof. Joseph S. Wall and Beth Yu Lin in U.S. Brookhaven National Laboratory. C.-A.L acknowledges the NSC Project Award for young scientist.

Supporting Information Available: Experimental section and supporting figures. SI.1: Synthesis and characterization of nanoparticles/protein corona; SI.1-1: General description; SI.1-2: Chemicals; SI.1–3: Synthesis of amphiphilic polymer; SI.1–4: Polymer coating of hydrophobic NPs; SI.1-5: Formation of self-assembled protein corona on polymer-coated NPs; SI.1-6: Characterization of self-assembled protein corona on polymer-coated NPs; SI.1-6a: Monolayered protein corona formation and reactivity; SI.1-6b: Estimating the quantities of BSA on the nanoparticles; SI.1-6c: Transmission electron microscope; SI.2: Synthesis of protein-caged fluorescent AuNCs; SI.2-1: General description; SI.2-2: Chemicals; SI.2-3: Synthesis of DHLA-protected AuNCs; SI.2-4: Synthesis of "biomineralized" protein-caged fluorescent AuNCs; SI.3: Synthesis and characterization of air-filled MBs from protein cage nanomaterials; SI.3-1: General description; SI.3-2: Synthesis of MBs from protein-caged fluorescent AuNCs; SI.3-3: Synthesis of MBs from nanoparticle–protein corona; SI.3-4: Flow cytometry analysis of fluorescent MBs; SI.4: Animal model and ethical approval for use of human blood; SI.4-1: Short-term and long-term stability of MBs in blood; SI.4-2: Cell viability analysis; SI.4-3: Experimental setup of ultrasound brain imaging; SI.5: Acoustic characterization of NC-coated microbubbles; SI.5-1: Stability of MBs under ultrasound exposure; SI.5-2: Nonlinear acoustic properties of MBs. This material is available free of charge *via* the Internet at http://pubs.acs.org.

REFERENCES AND NOTES

1. Thanh, N. T. K.; Green, L. A. W. Functionalisation of Nanoparticles for Biomedical Applications. *Nano Today* **2010**, *5*, 213–230.
2. Cai, W. B.; Chen, X. Y. Nanoplatforms for Targeted Molecular Imaging in Living Subjects. *Small* **2007**, *3*, 1840–1854.
3. Phillips, M. A.; Gran, M. L.; Peppas, N. A. Targeted Nanodelivery of Drugs and Diagnostics. *Nano Today* **2010**, *5*, 143–159.
4. Landsiedel, R.; Ma-Hock, L.; Kroll, A.; Hahn, D.; Schnekenburger, J.; Wiench, K.; Wohlleben, W. Testing Metal-Oxide Nanomaterials for Human Safety. *Adv. Mater.* **2010**, *22*, 2601–2627.
5. Lee, J. H.; Yigit, M. V.; Mazumdar, D.; Lu, Y. Molecular Diagnostic and Drug Delivery Agents Based on Aptamer-Nanomaterial Conjugates. *Adv. Drug Delivery Rev.* **2010**, *62*, 592–605.
6. Petros, R. A.; DeSimone, J. M. Strategies in the Design of Nanoparticles for Therapeutic Applications. *Nat. Rev. Drug Discovery* **2010**, *9*, 615–627.

7. Thorek, D. L. J.; Chen, A.; Czupryna, J.; Tsourkas, A. Superparamagnetic Iron Oxide Nanoparticle Probes for Molecular Imaging. *Ann. Biomed. Eng.* **2006**, *34*, 23–38.
8. Bruchez, M.; Moronne, M.; Gin, P.; Weiss, S.; Alivisatos, A. P. Semiconductor Nanocrystals As Fluorescent Biological Labels. *Science* **1998**, *281*, 2013–2016.
9. Chan, W. C. W.; Nie, S. M. Quantum Dot Bioconjugates for Ultrasensitive Nonisotopic Detection. *Science* **1998**, *281*, 2016–2018.
10. Lin, C.-A. J.; Yang, T. Y.; Lee, C. H.; Huang, S. H.; Sperling, R. A.; Zanella, M.; Li, J. K.; Shen, J. L.; Wang, H. H.; Yeh, H. I.; *et al*. Synthesis, Characterization, and Bioconjugation of Fluorescent Gold Nanoclusters toward Biological Labeling Applications. *ACS Nano* **2009**, *3*, 395–401.
11. Lin, C. A. J.; Lee, C. H.; Hsieh, J. T.; Wang, H. H.; Li, J. K.; Shen, J. L.; Chan, W. H.; Yeh, H. I.; Chang, W. H. Synthesis of Fluorescent Metallic Nanoclusters toward Biomedical Application: Recent Progress and Present Challenges. *J. Med. Biol. Eng.* **2009**, *29*, 276–283.
12. Shang, L.; Dong, S. J.; Nienhaus, G. U. Ultra-small Fluorescent Metal Nanoclusters: Synthesis and Biological Applications. *Nano Today* **2011**, *6*, 401–418.
13. Wang, H.-H.; Su, C.-H.; Wu, Y.-J.; Lin, C.-A. J.; Lee, C.-H.; Shen, J.-L.; Chan, W.-H.; Chang, W. H.; Yeh, H.-I. Application of Gold in Biomedicine: Past, Present and Future. *Int. J. Gerontol.* **2012**, *6*, 1–4.
14. Kim, D.; Park, S.; Lee, J. H.; Jeong, Y. Y.; Jon, S. Antibiofouling Polymer-Coated Gold Nanoparticles As a Contrast Agent for *in Vivo* X-ray Computed Tomography Imaging. *J. Am. Chem. Soc.* **2007**, *129*, 7661–7665.
15. Jaffer, F. A.; Libby, P.; Weissleder, R. Molecular Imaging of Cardiovascular Disease. *Circulation* **2007**, *116*, 1052–1061.
16. de Vries, I. J. M.; Lesterhuis, W. J.; Barentsz, J. O.; Verdijk, P.; van Krieken, J. H.; Boerman, O. C.; Oyen, W. J. G.; Bonenkamp, J. J.; Boezeman, J. B.; Adema, G. J.; *et al*. Magnetic Resonance Tracking of Dendritic Cells in Melanoma Patients for Monitoring of Cellular Therapy. *Nat. Biotechnol.* **2005**, *23*, 1407–1413.
17. Bulte, J. W. M.; Kraitchman, D. L. Iron Oxide MR Contrast Agents for Molecular and Cellular Imaging. *NMR Biomed.* **2004**, *17*, 484–499.
18. Wickline, S. A.; Neubauer, A. M.; Winter, P.; Caruthers, S.; Lanza, G. Applications of Nanotechnology to Atherosclerosis, Thrombosis, and Vascular Biology. *Arterioscl. Throm. Vas.* **2006**, *26*, 435–441.
19. Medintz, I. L.; Uyeda, H. T.; Goldman, E. R.; Mattoussi, H. Quantum Dot Bioconjugates for Imaging, Labelling and Sensing. *Nat. Mater.* **2005**, *4*, 435–446.
20. Kobayashi, H.; Hama, Y.; Koyama, Y.; Barrett, T.; Regino, C. A. S.; Urano, Y.; Choyke, P. L. Simultaneous Multicolor Imaging of Five Different Lymphatic Basins Using Quantum Dots. *Nano Lett.* **2007**, *7*, 1711–1716.
21. Michalet, X.; Pinaud, F. F.; Bentolila, L. A.; Tsay, J. M.; Doose, S.; Li, J. J.; Sundaresan, G.; Wu, A. M.; Gambhir, S. S.; Weiss, S. Quantum Dots for Live Cells, *in Vivo* Imaging, and Diagnostics. *Science* **2005**, *307*, 538–544.
22. Cai, W. B.; Shin, D. W.; Chen, K.; Gheysens, O.; Cao, Q. Z.; Wang, S. X.; Gambhir, S. S.; Chen, X. Y. Peptide-Labeled Near-Infrared Quantum Dots for Imaging Tumor Vasculature in Living Subjects. *Nano Lett.* **2006**, *6*, 669–676.
23. Massoud, T. F.; Gambhir, S. S. Molecular Imaging in Living Subjects: Seeing Fundamental Biological Processes in a New Light. *Gene Dev.* **2003**, *17*, 545–580.
24. Mulder, W. J. M.; Strijkers, G. J.; Habets, J. W.; Bleeker, E. J. W.; van der Schaft, D. W. J.; Storm, G.; Koning, G. A.; Griffioen, A. W.; Nicolay, K. MR Molecular Imaging and Fluorescence Microscopy for Identification of Activated Tumor Endothelium Using a Bimodal Lipidic Nanoparticle. *FASEB J.* **2005**, *19*, 2008–2010.
25. Montet, X.; Weissleder, R.; Josephson, L. Imaging Pancreatic Cancer with a Peptide-Nanoparticle Conjugate Targeted to Normal Pancreas. *Bioconjugate Chem.* **2006**, *17*, 905–911.
26. Sosnovik, D. E.; Schellenberger, E. A.; Nahrendorf, M.; Novikov, M. S.; Matsui, T.; Dai, G.; Reynolds, F.; Grazette, L.; Rosenzweig, A.; Weissleder, R.; Josephson, L. Magnetic Resonance Imaging of Cardiomyocyte Apoptosis with a Novel Magneto-Optical Nanoparticle. *Magn. Reson. Med.* **2005**, *54*, 718–724.
27. Nahrendorf, M.; Jaffer, F. A.; Kelly, K. A.; Sosnovik, D. E.; Aikawa, E.; Libby, P.; Weissleder, R. Noninvasive Vascular Cell Adhesion Molecule-1 Imaging Identifies Inflammatory Activation of Cells in Atherosclerosis. *Circulation* **2006**, *114*, 1504–1511.
28. Kelly, K. A.; Allport, J. R.; Tsourkas, A.; Shinde-Patil, V. R.; Josephson, L.; Weissleder, R. Detection of Vascular Adhesion Molecule-1 Expression Using a Novel Multimodal Nanoparticle. *Circ. Res.* **2005**, *96*, 327–336.
29. Cai, W. B.; Chen, K.; Li, Z. B.; Gambhir, S. S.; Chen, X. Y. Dual-Function Probe for PET and near-Infrared Fluorescence Imaging of Tumor Vasculature. *J. Nucl. Med.* **2007**, *48*, 1862–1870.
30. Mulder, W. J. M.; Koole, R.; Brandwijk, R. J.; Storm, G.; Chin, P. T. K.; Strijkers, G. J.; Donega, C. D.; Nicolay, K.; Griffioen, A. W. Quantum Dots with a Paramagnetic Coating As a Bimodal Molecular Imaging Probe. *Nano Lett.* **2006**, *6*, 1–6.
31. Tsourkas, A.; Shinde-Patil, V. R.; Kelly, K. A.; Patel, P.; Wolley, A.; Allport, J. R.; Weissleder, R. *in Vivo* Imaging of Activated Endothelium Using an Anti-VCAM-1 Magnetooptical Probe. *Bioconjugate Chem.* **2005**, *16*, 576–581.
32. Funovics, M.; Montet, X.; Reynolds, F.; Weissleder, R.; Josephson, L. Nanoparticles for the Optical Imaging of Tumor E-Selectin. *Neoplasia* **2005**, *7*, 904–911.
33. Zielhuis, S. W.; Seppenwoolde, J. H.; Mateus, V. A. P.; Bakker, C. J. G.; Krijger, G. C.; Storm, G.; Zonnenberg, B. A.; van het Schip, A. D.; Koning, G. A.; Nijsen, J. F. W. Lanthanide-Loaded Liposomes for Multimodality Imaging and Therapy. *Cancer Biother. Radio.* **2006**, *21*, 520–527.
34. Schutt, E. G.; Klein, D. H.; Mattrey, R. M.; Riess, J. G. Injectable Microbubbles As Contrast Agents for Diagnostic Ultrasound Imaging: The Key Role of Perfluorochemicals. *Angew. Chem., Int. Ed.* **2003**, *42*, 3218–3235.
35. Lentacker, I.; De Smedt, S. C.; Sanders, N. N. Drug Loaded Microbubble Design for Ultrasound Triggered Delivery. *Soft Matter.* **2009**, *5*, 2161–2170.
36. Lindner, J. R. Microbubbles in Medical Imaging: Current Applications and Future Directions. *Nat. Rev. Drug Discovery* **2004**, *3*, 527–532.
37. Cosgrove, D. Ultrasound Contrast Agents: An Overview. *Eur. J. Radiol.* **2006**, *60*, 324–330.
38. Sboros, V. Response of Contrast Agents to Ultrasound. *Adv. Drug Delivery Rev.* **2008**, *60*, 1117–1136.
39. Ferrara, K.; Pollard, R.; Borden, M. Ultrasound Microbubble Contrast Agents: Fundamentals and Application to Gene and Drug Delivery. *Annu. Rev. Biomed. Eng.* **2007**, *9*, 415–447.
40. Xie, F.; Tsutsui, J. M.; Lof, J.; Unger, E. C.; Johanning, J.; Culp, W. C.; Matsunaga, T.; Porter, T. R. Effectiveness of Lipid Microbubbles and Ultrasound in Declotting Thrombosis. *Ultrasound Med. Biol.* **2005**, *31*, 979–985.
41. Weller, G. E. R.; Villanueva, F. S.; Klibanov, A. L.; Wagner, W. R. Modulating Targeted Adhesion of an Ultrasound Contrast Agent to Dysfunctional Endothelium. *Ann. Biomed. Eng.* **2002**, *30*, 1012–1019.
42. Leong-Poi, H.; Christiansen, J.; Klibanov, A. L.; Kaul, S.; Lindner, J. R. Noninvasive Assessment of Angiogenesis by Ultrasound and Microbubbles Targeted to Alpha(v)-Integrins. *Circulation* **2003**, *107*, 455–460.
43. Cavalieri, F.; Finelli, I.; Tortora, M.; Mozetic, P.; Chiessi, E.; Polizio, F.; Brismar, T. B.; Paradossi, G. Polymer Microbubbles As Diagnostic and Therapeutic Gas Delivery Device. *Chem. Mater.* **2008**, *20*, 3254–3258.
44. Lentacker, I.; De Smedt, S. C.; Demeester, J.; Van Marck, V.; Bracke, M.; Sanders, N. N. Lipoplex-Loaded Microbubbles for Gene Delivery: A Trojan Horse Controlled by Ultrasound. *Adv. Funct. Mater.* **2007**, *17*, 1910–1916.
45. Lum, A. F. H.; Borden, M. A.; Dayton, P. A.; Kruse, D. E.; Simon, S. I.; Ferrara, K. W. Ultrasound Radiation Force Enables Targeted Deposition of Model Drug Carriers Loaded on Microbubbles. *J. Controlled Release* **2006**, *111*, 128–134.

46. Eisenbrey, J. R.; Burstein, O. M.; Kambhampati, R.; Forsberg, F.; Liu, J. B.; Wheatley, M. A. Development and Optimization of a Doxorubicin Loaded Poly(lactic acid) Contrast Agent for Ultrasound Directed Drug Delivery. *J. Controlled Release* **2010**, *143*, 38–44.
47. Huh, Y. M.; Jun, Y. W.; Song, H. T.; Kim, S.; Choi, J. S.; Lee, J. H.; Yoon, S.; Kim, K. S.; Shin, J. S.; Suh, J. S.; *et al*. In Vivo Magnetic Resonance Detection of Cancer by Using Multifunctional Magnetic Nanocrystals. *J. Am. Chem. Soc.* **2005**, *127*, 12387–12391.
48. Yang, F.; Li, Y. X.; Chen, Z. P.; Zhang, Y.; Wu, J. R.; Gu, N. Superparamagnetic Iron Oxide Nanoparticle-Embedded Encapsulated Microbubbles As Dual Contrast Agents of Magnetic Resonance and Ultrasound Imaging. *Biomaterials* **2009**, *30*, 3882–3890.
49. Ke, H.; Xing, Z. W.; Zhao, B.; Wang, J. R.; Liu, J. B.; Guo, C. X.; Yue, X. L.; Liu, S. Q.; Tang, Z. Y.; Dai, Z. F. Quantum-Dot-Modified Microbubbles with Bi-mode Imaging Capabilities. *Nanotechnology* **2009**, *20*, 425105.
50. Lee, M. H.; Prasad, V.; Lee, D. Microfluidic Fabrication of Stable Nanoparticle-Shelled Bubbles. *Langmuir* **2010**, *26*, 2227–2230.
51. Yang, F.; Li, L.; Li, Y. X.; Chen, Z. P.; Wu, J. R.; Gu, N. Superparamagnetic Nanoparticle-Inclusion Microbubbles for Ultrasound Contrast Agents. *Phys. Med. Biol.* **2008**, *53*, 6129–6141.
52. Cavalieri, F.; Ashokkumar, M.; Grieser, F.; Caruso, F. Ultrasonic Synthesis of Stable, Functional Lysozyme Microbubbles. *Langmuir* **2008**, *24*, 10078–10083.
53. Seo, M.; Gorelikov, I.; Williams, R.; Matsuura, N. Microfluidic Assembly of Monodisperse, Nanoparticle-Incorporated Perfluorocarbon Microbubbles for Medical Imaging and Therapy. *Langmuir* **2010**, *26*, 13855–13860.
54. Park, J. I.; Jagadeesan, D.; Williams, R.; Oakden, W.; Chung, S. Y.; Stanisz, G. J.; Kumacheva, E. Microbubbles Loaded with Nanoparticles: A Route to Multiple Imaging Modalities. *ACS Nano* **2010**, *4*, 6579–6586.
55. Liu, T. Y.; Hu, S. H.; Liu, D. M.; Chen, S. Y.; Chen, I. W. Biomedical Nanoparticle Carriers with Combined Thermal and Magnetic Responses. *Nano Today* **2009**, *4*, 52–65.
56. Park, K.; Lee, S.; Kang, E.; Kim, K.; Choi, K.; Kwon, I. C. New Generation of Multifunctional Nanoparticles for Cancer Imaging and Therapy. *Adv Funct. Mater.* **2009**, *19*, 1553–1566.
57. Kabalnov, A.; Klein, D.; Pelura, T.; Schutt, E.; Weers, J. Dissolution of Multicomponent Microbubbles in the Bloodstream: 1. Theory. *Ultrasound Med. Biol.* **1998**, *24*, 739–749.
58. Lin, C.-A. J.; Sperling, R. A.; Li, J. K.; Yang, T. Y.; Li, P. Y.; Zanella, M.; Chang, W. H.; Parak, W. G. J. Design of an Amphiphilic Polymer for Nanoparticle Coating and Functionalization. *Small* **2008**, *4*, 334–341.
59. Pellegrino, T.; Manna, L.; Kudera, S.; Liedl, T.; Koktysh, D.; Rogach, A. L.; Keller, S.; Radler, J.; Natile, G.; Parak, W. J. Hydrophobic Nanocrystals Coated with an Amphiphilic Polymer Shell: A General Route to Water Soluble Nanocrystals. *Nano Lett.* **2004**, *4*, 703–707.
60. Srivastava, S.; Verma, A.; Frankamp, B. L.; Rotello, V. M. Controlled Assembly of Protein-Nanoparticle Composites through Protein Surface Recognition. *Adv. Mater.* **2005**, *17*, 617–621.
61. De, M.; Miranda, O. R.; Rana, S.; Rotello, V. M. Size and Geometry Dependent Protein-Nanoparticle Self-Assembly. *Chem. Commun.* **2009**, 2157–2159.
62. Christiansen, C.; Kryvi, H.; Sontum, P. C.; Skotland, T. Physical and Biochemical-Characterization of Albunex(Tm), a New Ultrasound Contrast Agent Consisting of Air-Filled Albumin Microspheres Suspended in a Solution of Human Albumin. *Biotechnol. Appl. Biochem.* **1994**, *19*, 307–320.
63. Grinstaff, M. W.; Suslick, K. S. Air-Filled Proteinaceous Microbubbles: Synthesis of an Echo-Contrast Agent. *Proc. Natl. Acad. Sci. U. S. A.* **1991**, *88*, 7708–7710.
64. Zhou, M. F.; Cavalieri, F.; Ashokkumar, M. Tailoring the Properties of Ultrasonically Synthesised Microbubbles. *Soft Matter* **2011**, *7*, 623–630.
65. Wang, H. H.; Lin, C. A. J.; Lee, C. H.; Lin, Y. C.; Tseng, Y. M.; Hsieh, C. L.; Chen, C. H.; Tsai, C. H.; Hsieh, C. T.; Shen, J. L.; *et al*. Fluorescent Gold Nanoclusters As a Biocompatible Marker for *in Vitro* and *in Vivo* Tracking of Endothelial Cells. *ACS Nano* **2011**, *5*, 4337–4344.
66. Kirchner, C.; Liedl, T.; Kudera, S.; Pellegrino, T.; Javier, A. M.; Gaub, H. E.; Stolzle, S.; Fertig, N.; Parak, W. J. Cytotoxicity of Colloidal CdSe and CdSe/ZnS Nanoparticles. *Nano Lett.* **2005**, *5*, 331–338.
67. Derfus, A. M.; Chan, W. C. W.; Bhatia, S. N. Probing the Cytotoxicity of Semiconductor Quantum Dots. *Nano Lett.* **2004**, *4*, 11–18.
68. Xie, J. P.; Zheng, Y. G.; Ying, J. Y. Protein-Directed Synthesis of Highly Fluorescent Gold Nanoclusters. *J. Am. Chem. Soc.* **2009**, *131*, 888–889.
69. Sun, C. J.; Yang, H.; Yuan, Y.; Tian, X.; Wang, L. M.; Guo, Y.; Xu, L.; Lei, J. L.; Gao, N.; Anderson; *et al*. Controlling Assembly of Paired Gold Clusters within Apoferritin Nanoreactor for *in Vivo* Kidney Targeting and Biomedical Imaging. *J. Am. Chem. Soc.* **2011**, *133*, 8617–8624.
70. Cavalieri, F.; Zhou, M. F.; Ashokkumar, M. The Design of Multifunctional Microbubbles for Ultrasound Image-Guided Cancer Therapy. *Curr. Top. Med. Chem.* **2010**, *10*, 1198–1210.
71. Kim, C.; Qin, R. G.; Xu, J. S.; Wang, L. V.; Xu, R. Multifunctional Microbubbles and Nanobubbles for Photoacoustic and Ultrasound Imaging. *J. Biomed. Opt.* **2010**, 15,.
72. Chow, A. M.; Chan, K. W. Y.; Cheung, J. S.; Wu, E. X. Enhancement of Gas-Filled Microbubble R-2* by Iron Oxide Nanoparticles for MRI. *Magn. Reson. Med.* **2010**, *63*, 224–229.
73. Wu, X.; He, X. X.; Wang, K. M.; Xie, C.; Zhou, B.; Qing, Z. H. Ultrasmall near-Infrared Gold Nanoclusters for Tumor Fluorescence Imaging *in Vivo*. *Nanoscale* **2010**, *2*, 2244–2249.
74. Liu, Z.; Lammers, T.; Ehling, J.; Fokong, S.; Bornemann, J.; Kiessling, F.; Gatjens, J. Iron Oxide Nanoparticle-Containing Microbubble Composites As Contrast Agents for MR and Ultrasound Dual-Modality Imaging. *Biomaterials* **2011**, *32*, 6155–6163.
75. Yeh, C. K.; Su, S. Y. Effects of Acoustic Insonation Parameters on Ultrasound Contrast Agent Destruction. *Ultrasound Med Biol.* **2008**, *34*, 1281–1291.
76. Kang, S. T.; Yeh, C. K. A Maleimide-Based *in-Vitro* Model for Ultrasound Targeted Imaging. *Ultrason. Sonochem.* **2011**, *18*, 327–333.
77. Hernot, S.; Klibanov, A. L. Microbubbles in Ultrasound-Triggered Drug and Gene Delivery. *Adv. Drug Delivery Rev.* **2008**, *60*, 1153–1166.